RESEARCH ARTICLE

Magnetic Resonance in Medicine

Automatic segmentation and diameter measurement of deep medullary veins

Yichen Zhou[1] | Bingbing Zhao[1] | Julia Moore[2] | Xiaopeng Zong[1,3]

[1]School of Biomedical Engineering & State Key Laboratory of Advanced Medical Materials and Devices, ShanghaiTech University, Shanghai, China

[2]Massachusetts General Hospital, Boston, Massachusetts USA

[3]Shanghai Clinical Research and Trial Center, Shanghai, China

Correspondence
Xiaopeng Zong, School of Biomedical Engineering, ShanghaiTech University, Shanghai, China.
Email: zongxp@shanghaitech.edu.cn

Abstract

Purpose: As one of the pathogenic factors of cerebral small vessel disease, venous collagenosis may result in the occlusion or stenosis of deep medullary veins (DMVs). Although numerous DMVs can be observed in susceptibility-weighted MRI images, their diameters are usually smaller than the MRI resolution, making it difficult to segment them and quantify their sizes. We aim to automatically segment DMVs and measure their diameters from gradient-echo images.

Methods: A neural network model was trained for DMV segmentation based on the gradient-echo magnitude and phase images of 20 subjects at 7 T. The diameters of DMVs were obtained by fitting measured complex images with model images that accounted for the DMV-induced magnetic field and point spread function. A phantom study with graphite rods of different diameters was conducted to validate the proposed method. Simulation was carried out to evaluate the voxel-size dependence of measurement accuracy for a typical DMV size.

Results: The automatically segmented DMV masks had Dice similarity coefficients of 0.68 ± 0.03 (voxel level) and 0.83 ± 0.04 (cluster level). The fitted graphite-rod diameters closely matched their true values. In simulation, the fitted diameters closely matched the true value when voxel size was ≤ 0.45 mm, and 92.2% of DMVs had diameters between 90 μm and 200 μm with a peak at about 120 μm, which agreed well with an earlier ex vivo report.

Conclusion: The proposed methods enabled efficient and quantitative study of DMVs, which may help illuminate the role of DMVs in the etiopathogenesis of cerebral small vessel disease.

KEYWORDS
automatic segmentation, cerebral small vessel disease, deep medullary vein, venous diameter measurement

1 | INTRODUCTION

Deep medullary veins (DMVs) are parenchymal veins surrounding the lateral ventricle in human brain. Venous collagenosis, which may lead to the obstruction or stenosis of DMVs, has been proposed as one of the pathogenic factors of cerebral small vessel disease (CSVD).[1–3] Therefore, monitoring DMV diameter may shed new light into the mechanisms of CSVD.

Due to the relatively high magnetic susceptibility of venous blood, SWI and QSM techniques are often used for quantitative analysis of oxygen saturation and morphology of large cerebral veins.[4–7] However, when studying small cerebral veins such as DMVs (100–250 μm[8]), which is below the resolution limit of current human brain MRI, the partial-volume effect reduces the accuracy of QSM for quantitative measurement. Furthermore, due to the large numbers of DMVs in the brain, visual assessment of DMV morphology is time-consuming.[9–12] Only conventional semi-automatic segmentation methods based on thresholding, vesselness filter, and tubular tracking have been proposed to facilitate more efficient and quantitative DMV morphological assessment.[13–15] Given the remarkable performances of deep learning–based methods in small vessel segmentation,[16] it is highly desirable to develop neural network models to enable more accurate and fully automatic DMV segmentation.

Previous studies using SWI-based visual scoring of DMVs have revealed that decreased visibility and number of DMVs are associated with CSVD biomarkers such as white-matter (WM) hyperintensities in T_2-weighted MRI images and lacunar infarcts.[17,18] Quantitative measurement of DMV diameters may provide new insight into the role of DMVs in CSVD at an earlier stage. Multiple methods have been suggested to correct the partial-volume effect to achieve quantitative assessment of diameter, oxygen saturation, and/or the susceptibility of small vein.[19–21] However, none of these methods are suitable for the analysis of DMVs due to their smaller sizes and mostly perpendicular orientations relative to the main magnetic field.

Here, we aim to automatically segment DMVs through a neural network–based segmentation model and quantitatively measure the diameters of DMVs through physical model–based analysis of complex gradient-echo (GRE) images.

2 | THEORY

A DMV with nonzero blood-tissue susceptibility difference ($\Delta\chi$) in a magnetic field B_0 will generate an inhomogeneous magnetic field pattern. Modeling the DMV as a long cylinder, the local magnetic field experienced by the water protons inside the vessel with an angle θ_{vessel} relative to B_0 can be described as follows[21–23]:

$$\Delta B_{in} = B_0 \cdot \Delta\chi \cdot \frac{(3\cos^2\theta_{vessel} - 1)}{6} \qquad (1)$$

The field at point p outside DMV can be approximated by the sum of dipolar fields[24] produced by short segments of blood vessel, as follows:

$$\Delta B_{out,p} = \frac{\mu_0}{4\pi} \sum_{i=1}^{n} \frac{m_i(3\cos^2\theta_{ip} - 1)}{r_{ip}^3} \qquad (2)$$

where $m_i = \pi B_0 \Delta\chi a^2 l_i / \mu_0$ is the magnetic moment of vessel segment i; μ_0 is the magnetic permeability of free space; r_{ip} is the length of the line from point p to the center of the vessel segment i, and θ_{ip} is the angle between B_0 and this line; and a and l_i are the radius and length of segment i, respectively. In order for Eq. (2) to be valid, the segment length should satisfy $l_i \ll r_{ip}$ for most grid points p. In this study, we set $n = 50$ to divide the DMV into 50 short segments equally along its path. For a typical straight DMV length of about 5 mm, this results in $l_i = 0.1$ mm, which is much smaller than the voxel size and vessel length. Increasing n further was found not to alter the fitted DMV diameters, but resulted in longer computation time. A schematic diagram of the cylindrical DMV model is shown in Figure 1A.

The magnetic field inside and outside the vessel causes phase shift at any point p and results in complex signal intensity in GRE images as follows[25]:

$$\hat{S}_p = \begin{cases} m_{wm} \equiv^{i\gamma \cdot TE \cdot \Delta B_{out,p}} & (r_{ip} > a) \\ m_{blood} \equiv^{i\gamma \cdot TE \cdot \Delta B_{in}} & (r_{ip} \leq a) \end{cases} \qquad (3)$$

where γ is the gyromagnetic ratio, and m_{wm} and m_{blood} are the MR signal magnitudes in WM and the blood, respectively.

Assuming a voxel contains only a single DMV, the measured MRI signal in a voxel is the convolution of this complex signal with a 3D point spread function PSF(x, y, z), where the PSF function in each dimension is given by[19]
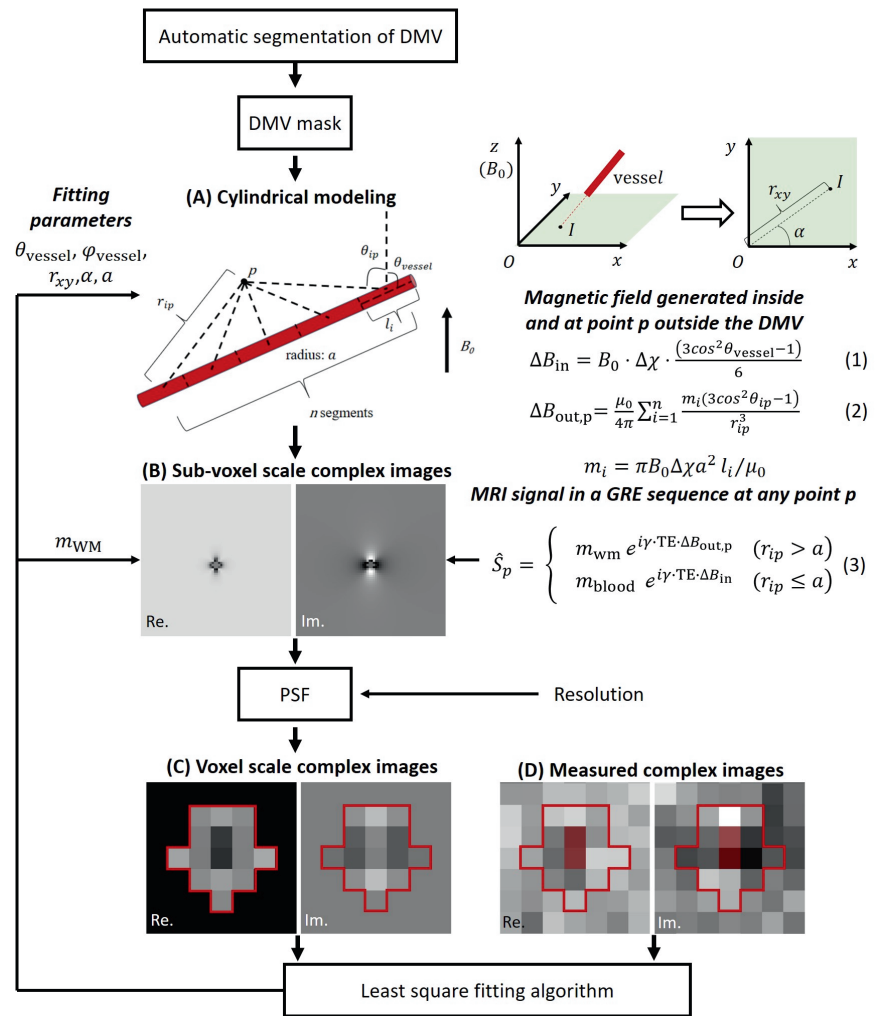
$$PSF(x) = \begin{cases} \frac{\Delta k}{2\pi} \cdot \frac{\sin(N \cdot \Delta k \cdot x/2)}{\sin(\Delta k \cdot x/2)}, x \neq 0 \\ N \cdot \frac{\Delta k}{2\pi}, x = 0 \end{cases} \qquad (4)$$

$$\Delta k = \frac{2\pi}{N \cdot \text{voxel size}} \qquad (5)$$

where N is the number of acquired k-space points.

The convoluted signal is sampled at the coordinates of the voxel centers and fitted to the measured voxel signals

FIGURE 1 Flow chart of the proposed method. (A) Diagram of the cylinder model (θ_{vessel} is the angle between vessel and B_0; μ_0 is the magnetic permeability of free space; r_{ip} is the length of the line from point p to the center of the vessel segment I, and θ_{ip} the angle between B_0 and this line; l_i is the length of vessel segment i; and a is the vessel radius). (B) Simulated complex images in subvoxel scale following Eqs. (1)-(3). (C) Simulated complex images after convolution with point spread function (PSF). (D) Measured complex images obtained from the gradient-echo (GRE) magnitude and phase images following Eq. (3); locations of deep medullary vein (DMV) mask voxels are labeled in red. The red contours in (C) and (D) represent the region of interest for nonlinear least-squares fitting.

via least-squares fitting. There are six fitting parameters, including θ_{vessel}, φ_{vessel}, r_{xy}, α, m_{wm}, and the vessel radius a. To ensure convergence of the fit, the values of $\Delta\chi$ and m_{blood} are fixed. The values of θ_{vessel}, φ_{vessel}, r_{xy}, and α are used to define the spatial position of the DMV axis, where φ_{vessel} is the azimuthal angle of the DMV about B_0, and α and r_{xy} are the angular position and distance to the origin of the intercept of the DMV axis on the x-y plane. The cost function is the sum of square of the modulus of the difference between measured and model-predicted complex MRI signals over voxels within a cylindrical region surrounding the longest straight segment of a DMV. The overall flow chart of the proposed method is illustrated in Figure 1.

3 | METHODS

3.1 | Graphite phantom study

To verify the proposed method, an MRI phantom was constructed, which consists of a plastic cylindrical container with a diameter of 55 mm and a height of 165 mm and a 2×4 array of graphite rods with different diameters (measured as 0.32, 0.32, 0.32, 0.54, 0.54, 0.55, 0.69, and 0.70 mm using a vernier caliper) uniformly placed in the container parallel to each other and to the bottom surface. The container was filled with tap water and sealed. The graphite rods (2B pencil leads) were made of 74% graphite, 20% clay, and 5% wax.[26]

The phantom was scanned on a 3T MR scanner (uMR890; United Image Healthcare, Shanghai, China) equipped with a 64-channel head receiver coil. The long axis of the cylindrical container and the graphite rods were parallel and perpendicular to the main magnetic field, respectively. A 3D multi-echo GRE sequence was performed with the following parameters: FOV = $150 \times 180 \times 216$ mm³; matrix size = $208 \times 250 \times 300$; spatial resolution = $0.72 \times 0.72 \times 0.72$ mm³; TR = 28.6 ms; TE1–TE7 = 3.7, 6.9, 10, 13, 17, 20, and 23 ms; flip angle (FA) = 15°; bandwidth = 350 Hz/pixel; undersampling factor = 4; and scan time = 7 min 47 s. The images were reconstructed using hybrid deep learning and iterative reconstruction.[27]

3.2 | In vivo study

The study was approved by the Institutional Review Board of the University of North Carolina at Chapel Hill. Twenty healthy volunteers aged between 21 and 55 years who provided written informed consents were scanned on a 7T Siemens Magneton MRI scanner using a Nova RF coil with 8 channels for transmitting and 32 channels for receiving. A 3D double-echo GRE-based SWI sequence was performed with the following parameters: $FOV = 220 \times 179 \times 83\,mm^3$; GRAPPA factor = 3 along phase-encoding direction; number of autocalibration signal lines = 30; matrix size = $512 \times 416 \times 208$; spatial resolution = $0.43 \times 0.43 \times 0.4\,mm^3$; TR = 21 ms; TE1/TE2 = 7.59/15 ms; FA = 10°; and scan time = 8 min 39 s. To avoid modification of the PSF in Eq. (4), all filters on the scan user interface that could affect the PSF during image reconstruction were turned off, including image filter, raw filter, and elliptical filter. The background phase on the phase images had been removed during SWI postprocessing by vendor software on the scanner. Because the background-phase removal only focuses on slow spatial phase variations, it should have minimal effect on the highly localized phase patterns associated with DMV. The scans were performed in the same experimental session as another study, which focused on studying the age dependence of the perivascular space morphology.[28] Only images without severe motion artifacts are included in this study.

3.3 | Automatic DMV segmentation

A 3D-UNet model provided by the nnU-Net framework was adopted to automatically segment DMVs.[29] To provide training data for the model, DMV masks were manually labeled on the GRE magnitude images acquired at TE2. We used images at TE2 for DMV segmentation, because DMVs were better visualized in images at the longer TE. To maximize the model performance in regions with the most DMV, the model input consisted of 64-slice axial slabs above the lateral ventricle, which contained the most DMVs approximately perpendicular to the main magnetic field. Both the magnitude and phase images acquired at TE2 were used as model input. Because DMVs are hypointense on the GRE magnitude images, contrasts of the input magnitude images were reversed before serving as model input, although this is not necessary.

To evaluate the performance of the segmentation model, we took 19 subjects as the training set, and the remaining subject as the test set, then repeated the process with each subject serving as the test set (20 combinations in all). Based on the test results, three metrics including

Dice similarity coefficient (DSC), sensitivity (SEN), and positive prediction value (PPV) were calculated as follows:

$$DSC = \frac{2TP}{2TP + FP + FN}$$

$$SEN = \frac{TP}{TP + FN}$$

$$PPV = \frac{TP}{TP + FP}$$

where TP, FP, and FN denote the true positive, false positive, and false negative DMV voxels or spatially connected DMV clusters, respectively. DMV clusters were defined as spatially connected DMV voxels, where all voxels on the eight vertices of a unit cube of the image grid are considered connected. DMV clusters with less than 4 voxels were excluded. When defined in terms of clusters, if a predicted vessel cluster spatially overlapped with a cluster in the ground-truth mask, it was considered as a true cluster. The cluster-based metrics were calculated, because the segmentation task was designed to reveal the approximate location of the DMVs and the diameter quantification was performed for each cluster instead of for each voxel.

3.4 | Simulation

To study the effect of spatial resolution on measurement accuracy, we applied the diameter quantification method to simulated GRE images of a DMV at different voxel sizes. The DMV had a length of 4 mm and a typical diameter of 0.15 mm, and was oriented perpendicular to the main magnetic field. The values of $\Delta\chi$, m_{blood}, and m_{wm} were set according to typical values in the in vivo study and were equal to 0.41 ppm, 17, and 60, respectively. Based on those values, the complex signal inside and outside of the vessel with TE = 15 ms and $B_0 = 7$ T was calculated according to Eqs. (1)-(3) at a grid spacing of $0.04 \times 0.04 \times 0.04\,mm^3$, where the summation in Eq. (2) was carried out over 100 evenly divided DMV segments of length 0.04 mm. Then complex Gaussian noise was added to the image. The SDs of the noise were chosen such that the SNR of WM at 0.4-mm voxel size was consistent with the SNR of our in vivo images (SNR = 10), and SNR is proportional to the voxel volume. We simulated a total of 11 isotropic voxel sizes between 0.08 and 1 mm by convolving the complex image with the PSF in Eq. (4). The convolution was performed at the same grid spacing as given previously. The simulated images had a size of $6 \times 6 \times 6\,mm^3$. This procedure was repeated 50 times with different Gaussian noise at each spatial resolution for calculating the random error.

3.5 | Data analysis
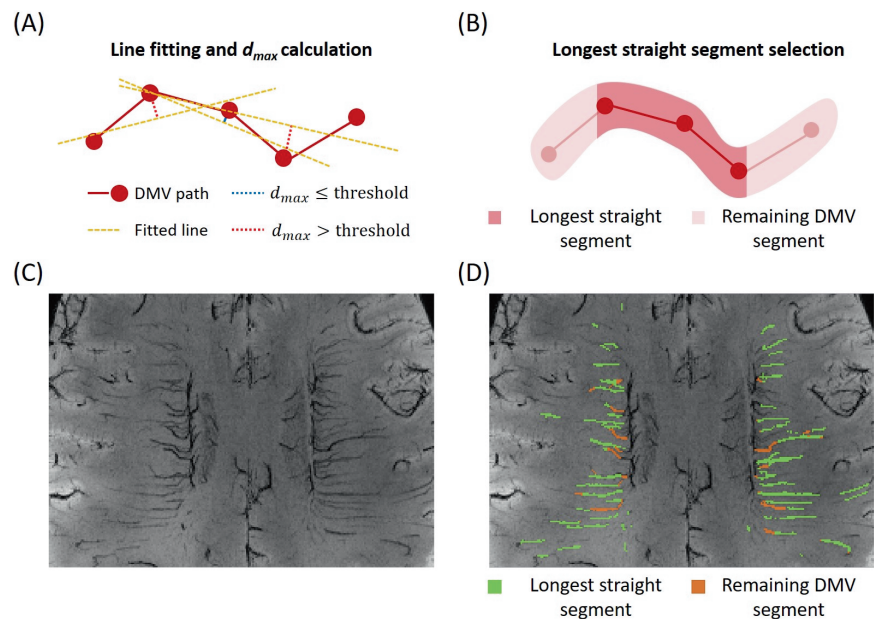
3.5.1 | Phantom study

In the phantom study, graphite rod masks with a total length of 10.5 mm were manually drawn based on the magnitude image acquired at TE1. They included all hypointense voxels on the image relative to the background. The principal component analysis algorithm[30] was applied to the matrix consisting of rows of mask voxel coordinates to obtain the initial direction of the rod. The initial values of θ_{vessel} and φ_{vessel} r_{xy} α were set as those for a line that was oriented in the main direction determined by principal component analysis and passed through the mean coordinates of all mask voxels. The region of interest (ROI) for model fitting was defined as a cylinder with a diameter of 9.4 mm, whose axis coincided with the line, had a length of 5.3 mm, and covered the middle half of the manually drawn mask.

The complex image was calculated from the magnitude image at TE1 and the phase difference image provided by the vendor. We used phase-difference image instead of the original phase image acquired at TE1 to remove the initial nonzero phase at TE = 0 ms. The phase difference is converted to the phase at TE1 by multiplying it by TE1/ΔTE before being used for model fitting. The image at the shortest TE (i.e., TE1) was used for model fitting, as the magnitude image had the least dark regions that extend beyond the actual space occupied by the rod. To obtain the model image, convolution between the modeled MR signal and the PSF were carried out for a cuboid enclosing this cylindrical ROI and had a dimension of $9.4 \times 9.4 \times 5.3 \text{ mm}^3$. The cuboid is discretized on a grid with spacing that is

one-tenth the MRI voxel size. Then, the complex signal and the PSF defined in Eq. (4) were convoluted on the same grid to obtain the model image. The value of m_{blood} was set to 0, because there were no water molecules in the graphite rods. Because the graphite rods we used (2B pencil leads) were made up of graphite powder, clay and wax, in which the graphite particles were evenly distributed in different orientations, they would exhibit isotropic magnetic susceptibility. As $\Delta\chi$ is unknown for the graphite rods, we assumed different $\Delta\chi$ values in the range of 40–120 ppm during model fitting.

3.5.2 | In vivo study

For the in vivo images, clustering was carried out on the segmented DMV masks from all test images. Because the DMV is assumed to be a straight line, the following procedure was used to find the longest straight segment of the line. First, a path is defined for each DMV cluster. The path is defined as the shortest path connecting the two terminal voxels in each cluster. Second, we performed line fitting on all path segments and the maximum distance (d_{max}), from the path segment voxels to the corresponding fitted lines was calculated. Finally, the longest path segment with d_{max} smaller than a preset threshold, was selected as the longest straight DMV segment. The procedure of searching for the longest straight segment and defining d_{max} are illustrated in Figure 2A,B. All voxels within a 2-mm-diameter cylinder whose axis coincided with the fitted line to the longest straight segment were included in the model fitting. Similar to the phantom study, the convolution was calculated for a cuboid enclosing the cylinder

FIGURE 2 Diagrams and demonstration of the straight-segment selection for deep medullary vein (DMV). (A) Line fitting and d_{max} calculation for DMV path segments. (B) Selection of the longest straight DMV segment based on the longest path segment with $d_{max} \leq$ threshold. (C) A zoomed area of the minimum intensity projection of the gradient-echo magnitude image. (D) Overlaid masks of the selected longest straight DMV segment as shown in green and the remaining DMV mask voxels as shown in orange after choosing the threshold of 0.5 mm for d_{max}.

and had a dimension of $2.0 \times 2.0 \times (1.6 + L)$ mm^3, where L is the length of the longest segment.
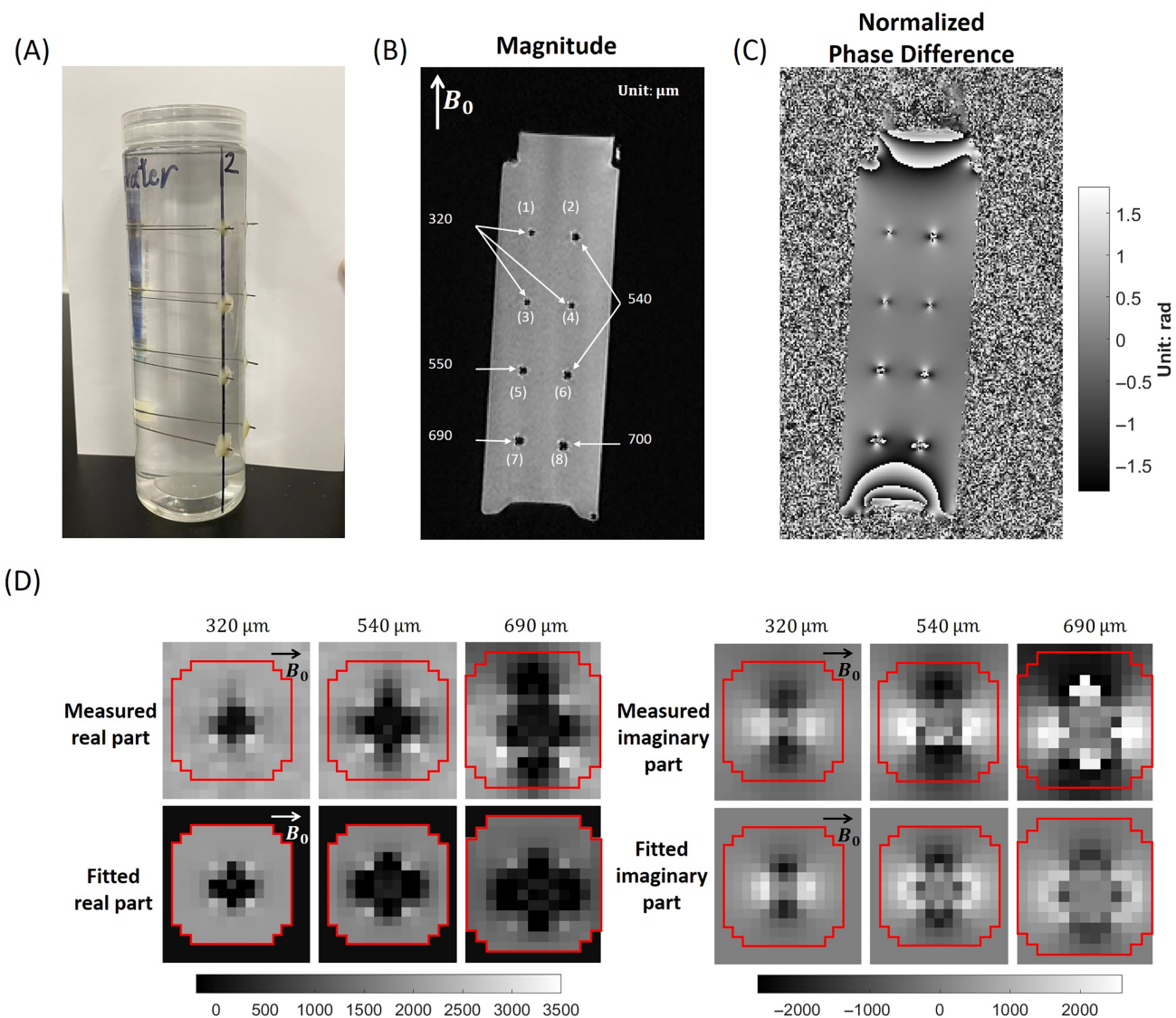
To determine the d_{max} for identifying the longest straight segment in a DMV, Figure 2C,D shows a zoomed area of the minimum intensity projection of GRE magnitude image at TE2 across 10 slices of a representative subject. The green voxels in Figure 2D had $d_{max} \leq 0.5$ mm, which matched the visually determined straight segments of DMVs well. Therefore, a distance threshold of 0.5 mm was adopted.

Model fitting was performed on the complex image at TE2. The central voxels of the thalamostriate vein (~110 voxels across three axial slices), which was not affected by partial volume effect, were manually labeled on the magnitude image at TE2, and m_{blood} was set as the mean magnitude of the labeled voxels during the fitting. The value of $\Delta\chi$ was set as 0.41 ppm, which was typical for cerebral veins.[20]

3.5.3 | Simulation

For the simulated images, the ROI for model fitting was defined as a cylinder whose axis coincided with the simulated vessel axis and had the same length as the vessel. The diameter of the cylinder was adjusted for each voxel

FIGURE 3 (A) A photo of the eight-graphite-rod phantom. (B) Gradient-echo magnitude image of the phantom. Arrows mark the true diameters of individual graphite rods. The index of each graphite rod is shown in parentheses. (C) Phase-difference image normalized to TE1. (D) The first and second rows on the left (right) are the measured and fitted real (imaginary) parts of the complex image surrounding three representative graphite rods in the cross-sectional plane. The true diameters of the rods are given at the top of each column. Only voxels within the red contour were used for fitting. The value of $\Delta\chi$ was assumed to be 83.5 ppm during fitting.

size to cover all voxels with visible phase difference from the background. The cuboid for convolution calculation, for obtaining the model image, coincided with the FOV of the simulated image.

All model fitting was performed in *MATLAB* R2020b (MathWorks, Natick, MA, USA) on a Windows personal computer equipped with Intel Core i5-11500U CPU and 16 GB RAM. Model fitting for each graphite rod took, on average, 670 s. The fitting time for each DMV depended on the length of the longest straight segment, which was between 80 and 3800 s with DMV path length ranging from 4 to 40 voxels.
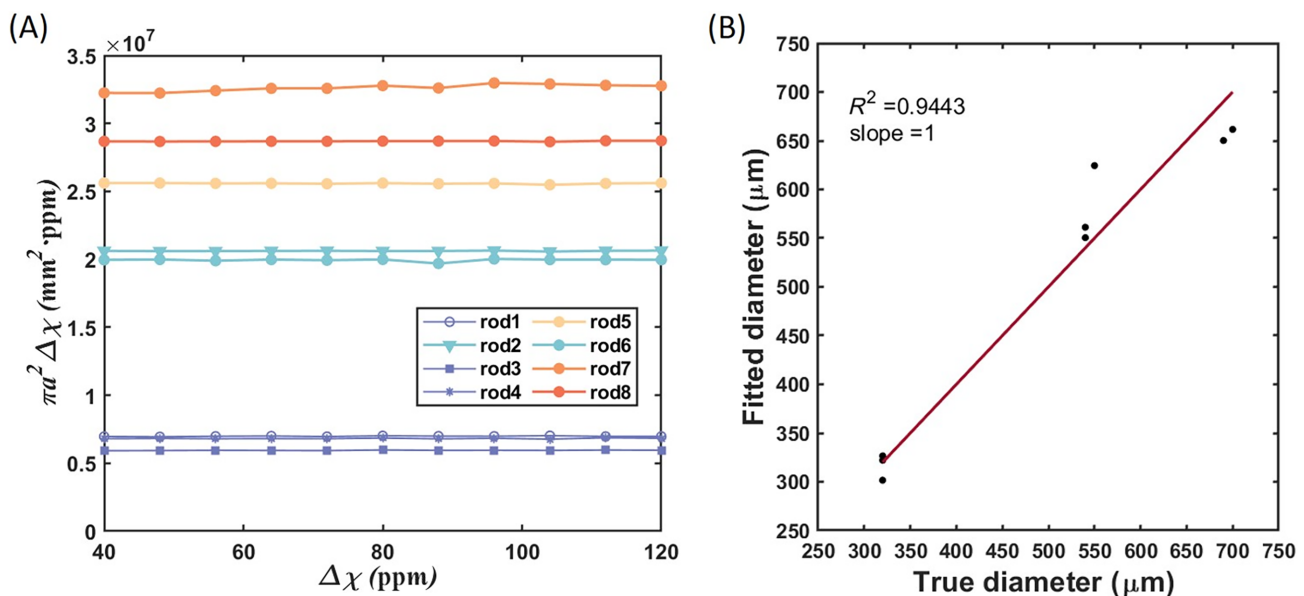
4 | RESULTS

A photo of the graphite phantom is shown in Figure 3A. Figure 3B shows a slice of the GRE magnitude image. The slice is perpendicular to graphite rods, and true diameters and rod indices are labeled for each rod. Figure 3C shows the corresponding phase-difference image after conversion to the phase at TE1. The dipole field distribution pattern can be clearly observed. There were also strong phase variations at the bottom and top of the phantom due to field inhomogeneity near the phantom–air interface. Figure 3D shows the measured and fitted real and imaginary parts of the complex image near the graphite rods with measured diameters of 320, 540, and 690 μm,

respectively. The fitted and measured images exhibit similar spatial patterns.

The product of $\Delta \chi$ and the fitted cross-sectional area ($= \pi a^2$) remained almost constant for different $\Delta \chi$, as illustrated in Figure 4A. The deviations of the product to their mean values ranged from -1.27% to 1.07%. When $\Delta \chi$ is assumed to be 83.5 ppm, the slope of the linear regression line with zero intercept is equal to 1 and R-square of the fit is 0.9443, as shown in Figure 4B. Because the fitted diameters scale with $1/\sqrt{\Delta \chi}$, the strong correlation will remain the same if a different $\Delta \chi$ value is assumed, although the slope of the linear regression line will deviate from unity.
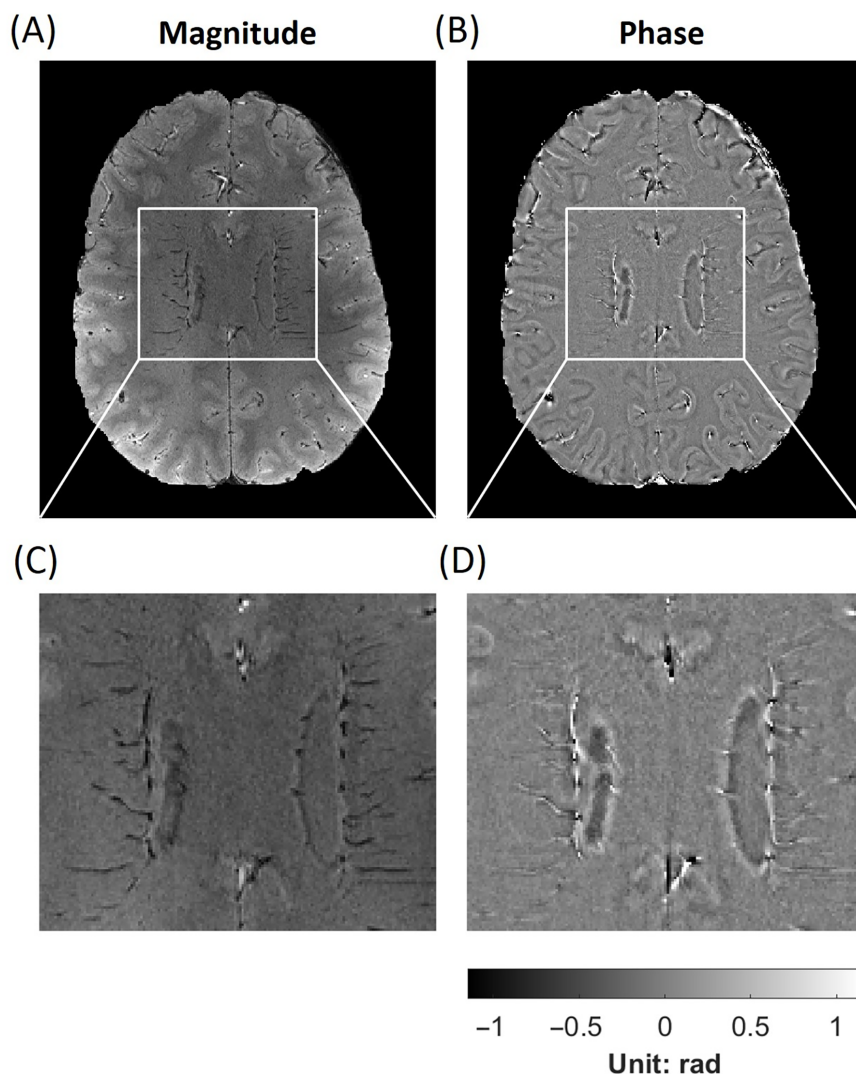
Figure 5A,B shows representative in vivo GRE magnitude and phase images at TE2 with non–brain tissue removed. Figure 5C,D shows the corresponding zoomed brain area where DMVs are densely distributed. DMVs can be identified as hypointense voxels on the magnitude image. However, the phase image has both hyperintense and hypointense voxels along the DMV path due to the dipolar field pattern induced by the DMVs.

Figure 6A,B shows a representative GRE magnitude image at TE2 and overlaid DMV masks generated by the trained nnU-Net model (labeled as green). Most DMV voxels that are hypointense within the WM are delineated by the segmentation model. A few DMV voxels remain undetected by the model (labeled as red), possibly due to their far distance from the lateral ventricle or close proximity to thalamostrate veins, which deviates from the

FIGURE 4 Fitting results of graphite rods in phantom. (A) The relationship between the product of the cross-sectional area of each graphite rod obtained by the fitted model and $\Delta \chi$ and the assumed susceptibility difference between water and graphite ($\Delta \chi$). (B) The scatter plot of the fitted and true diameters. The red line is a linear regression with zero intercept. The value of $\Delta \chi$ is assumed to be 83.5 ppm, such that the slope of the fitted line is equal to 1.

FIGURE 5 Representative in vivo gradient-echo images. (A) Magnitude image. (B) Phase image. (C,D) Zoomed brain area of magnitude image and phase image respectively.
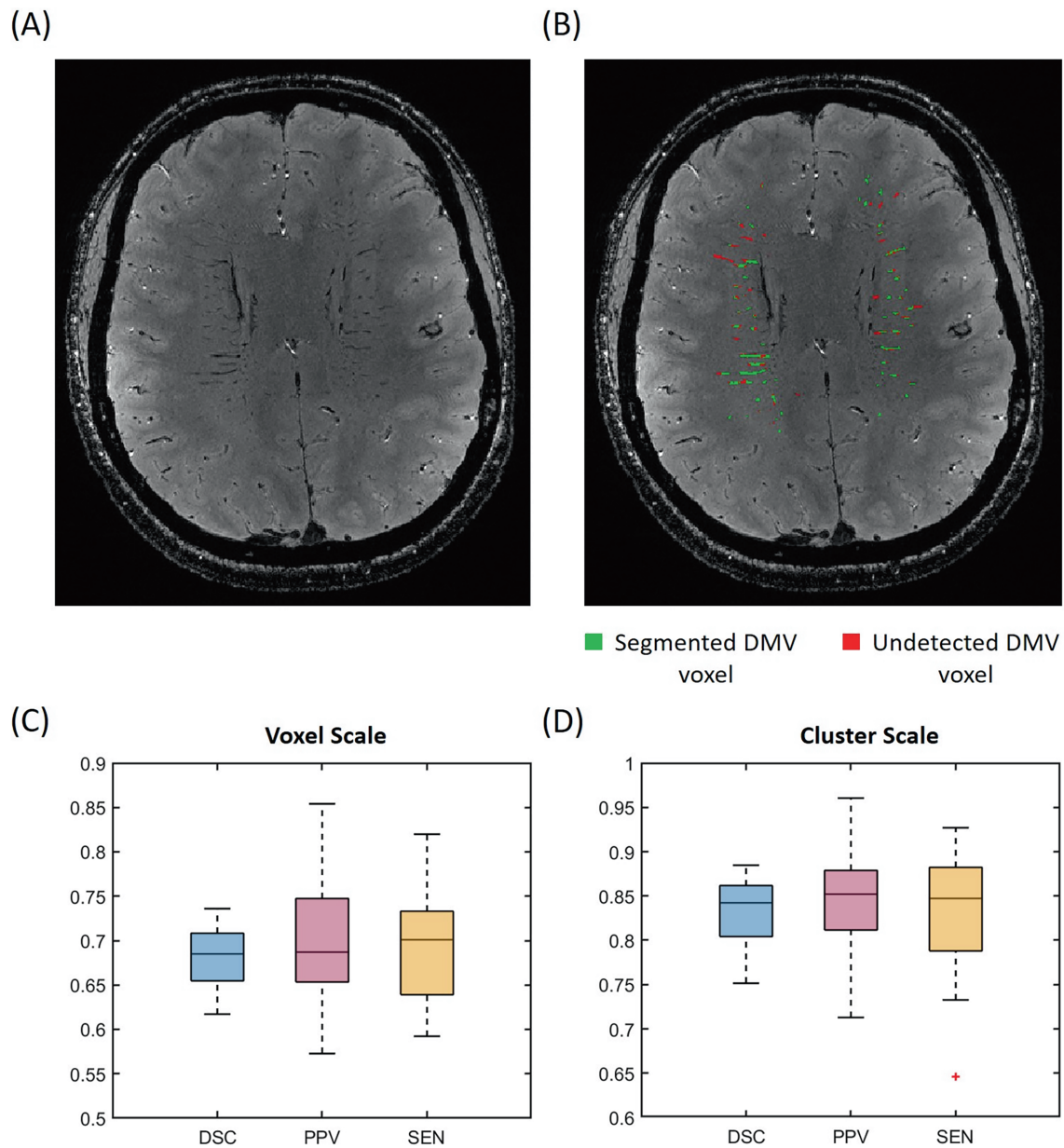
contextual features of most DMVs. On average, there are 136 DMVs on the 64 slices in each subject. In comparison, there are 151 DMVs on the 64 slices in the ground-truth mask. Figure 6C,D shows the DSC, PPV, and SEN values of the trained segmentation model evaluated on the voxel and cluster level across all 20 testing subjects. The mean and SDs of the DSC, PPV, and SEN are provided in Table 1. The longest straight segment ranged between 1.60 and 8.80 mm (mean $\pm$ SD: 4.64 ± 2.47 mm).

Figure 7A shows a zoomed minimum intensity projection image across three slices of a GRE magnitude image at TE2, with a white contour marking a representative DMV. Figure 7B shows the corresponding zoomed area of the representative DMV. Figure 7C shows the measured and fitted real and imaginary parts of the complex signal at TE2 of four continuous sagittal slices along the slice order defined in Figure 7B surrounding the representative DMV. Similar to the phantom images in Figure 3D, the fitted and measured images exhibited similar spatial patterns.

Figure 8A,B shows the zoomed minimum intensity projection images across five slices of a representative GRE magnitude image at TE2 and overlaid colormap of fitted diameters. Figure 8C illustrates the distribution of the fitted diameters of 2712 DMV clusters across all 20 subjects. Most of these fitted DMV diameters fell within the range of 90–200 μm with a peak at about 120 μm, encompassing 2501 (92.22%) DMV clusters. A total of 128 (4.72%) and 83 DMV clusters (3.06%) had fitted diameters less than 90 μm and exceeding 200 μm, respectively.

Figure 9A shows the simulated magnitude and phase images without PSF effects and at 0.12-mm, 0.24-mm, and 0.40-mm voxel sizes, respectively. As shown in Figure 9B, when the voxel size is less than or equal to 0.45 mm, the proposed model can estimate the diameter of the numerical vessel accurately (maximum absolute error = 8.66% at 0.45-mm voxel size). However, when the voxel size is ≥ 0.5 mm, the estimated vessel diameter has large errors (minimum absolute error = 23.33% at 0.5-mm voxel size).
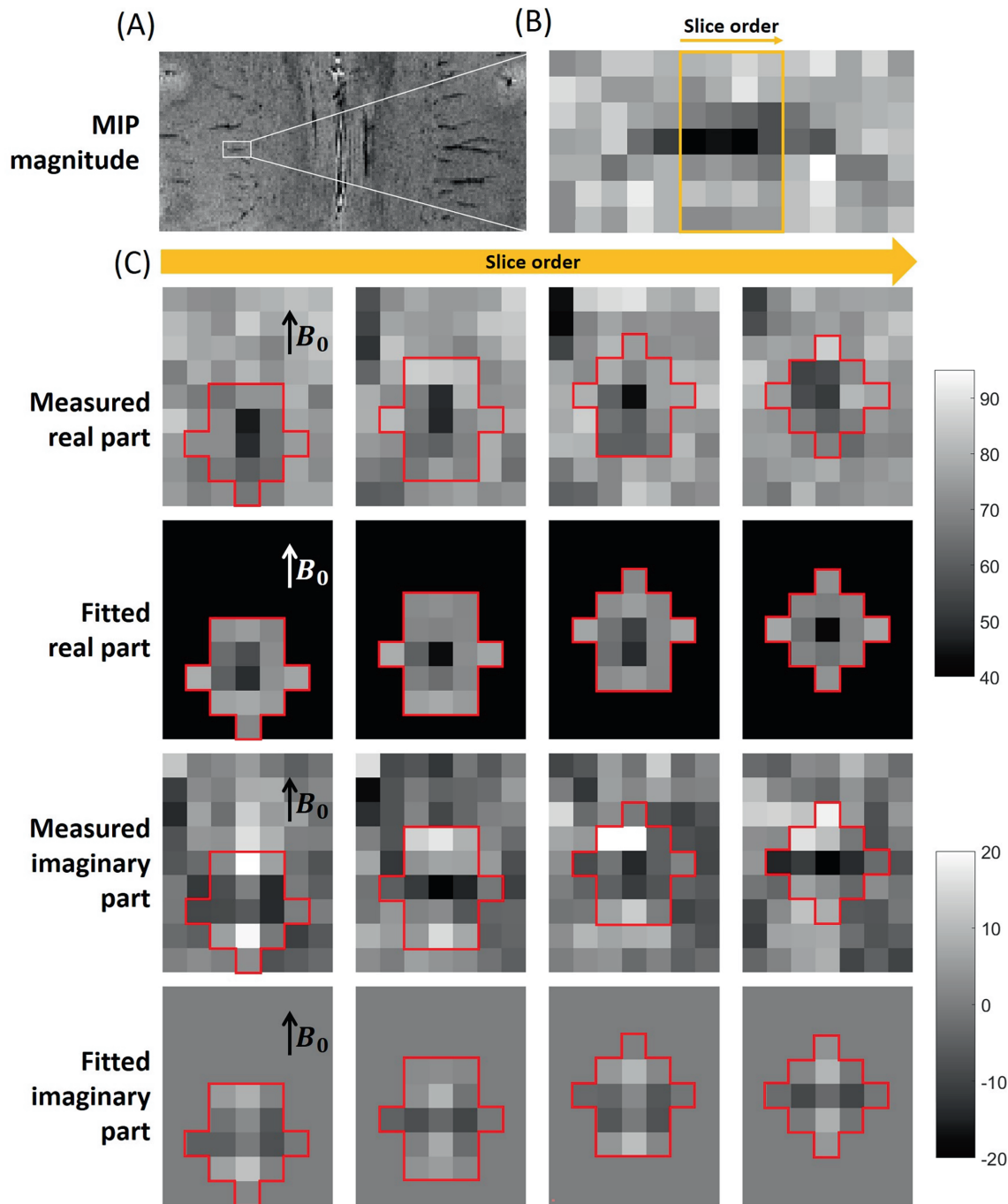
(A)

(B)

FIGURE 6 Segmented deep medullary vein (DMV) masks and evaluation metrics. (A) Representative gradient-echo magnitude image. (B) Overlaid DMV mask with green represented as nnU-Net segmented voxels and red represented false-negative DMV voxels. (C,D) Boxplots of Dice similarity coefficient, the sensitivity, and the positive prediction value of the DMV masks on voxel (C) and cluster (D) levels.

TABLE 1 The mean (SD) of the Dice similarity coefficient (DSC), positive prediction value (PPV), and sensitivity (SEN) values of deep medullary vein masks obtained by the nnU-Net segmentation of gradient-echo magnitude and phase images across all the 20 subjects on voxel and cluster scale.

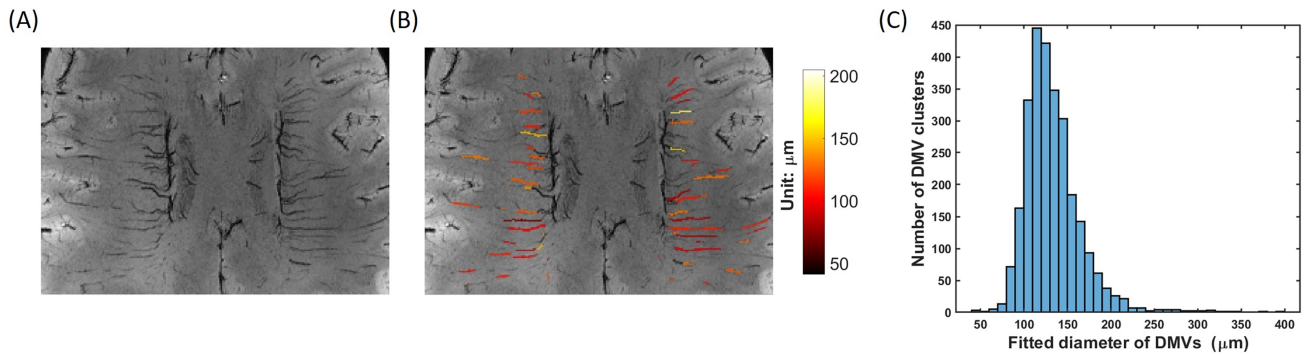|	DSC	PPV	SEN
Voxel scale	0.68 (0.03)	0.70 (0.07)	0.68 (0.08)
Cluster scale	0.83 (0.04)	0.84 (0.05)	0.83 (0.08)

FIGURE 7 (A) A zoomed area of the minimum intensity projection (MIP) of the gradient-echo magnitude image. The white contour marks a representative deep medullary vein (DMV). (B) The zoomed area of the representative DMV. (C) From left to right shows four successive slices along the slice order as defined in (B). From top to bottom shows the measure real parts, fitted real parts, measured imaginary parts, and fitted imaginary parts respectively. Only voxels within the red contour were used for fitting.
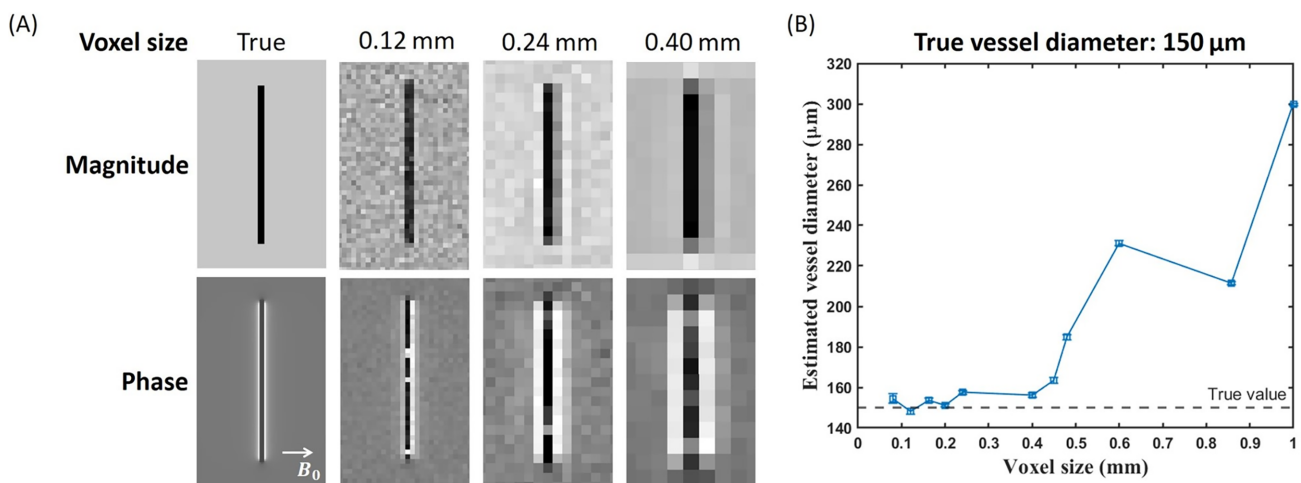
5 | DISCUSSION

In this study, we proposed a new method for quantitative study of DMVs, which consists of deep learning–based automatic segmentation and model-based quantitative measurement of DMV diameters. The trained segmentation model is able to segment 83% of the visible DMV with a positive prediction value of 84% and DSC of 83%. The validity of the model-based diameter quantification method was demonstrated in phantom experiments in which the measured diameter varied in proportion to the true diameter. We further applied our method to

FIGURE 8 Deep medullary vein (DMV) diameter fitting results. (A) Zoomed area of the minimum intensity projection of representative gradient-echo (GRE) magnitude image. (B) Color map of fitted DMV diameters overlaid on the minimum intensity projection of the GRE magnitude image. (C) Histogram of the fitted DMV diameters.

FIGURE 9 (A) *First column*: The magnitude and phase images used for simulations. *Second–fourth columns*: Representative magnitude and phase images simulated at voxel sizes of 0.12, 0.24, and 0.40 mm, respectively. (B) The vessel diameters estimated by the proposed model for all the simulated voxel sizes.

obtain diameters of the straight section of DMVs in vivo. The measured DMV diameters are in good accordance with ex vivo results measured using X-ray radiography.[8]

Several methods have been proposed for the segmentation of DMVs. Kuijf et al.'s segmentation method[13] first extracted the lateral ventricle from T_1-weighted (T1w) images, using its expanded surface as the ROI. Within this ROI on GRE images, a combination of vesselness filter, tubular tracking, and thresholding was applied to detect DMVs. Yan et al.[14] set a threshold based on the intensity of the brain parenchyma for initial segmentation of DMVs based on SWI images and manually removed false DMVs by an experienced radiologist. Jeong et al.[15] quantitatively analyzed the likelihood of a voxel being a vessel on SWI images based on association potentials such as intensity, tubular shape, and location, and then extracted DMVs from the WM regions defined on T1w images. Our study represents the first use of neural network models

in automatic DMV segmentation. There are two advantages of our nnU-Net-based DMV segmentation method over previous methods: First, only GRE magnitude and phase images are needed for segmentation, thus avoiding the errors that may be introduced by aligning T1w images with GRE/SWI. Second, our segmentation process is more concise and automated, requiring only automated preprocessing and 3D U-Net segmentation based on nnU-Net framework, without the need for manual setting of segmentation parameters. Overall, our deep learning–based DMV segmentation method is easier to deploy. It is noteworthy that when dealing with GRE data acquired under different acquisition conditions such as different TE, resolution, or field strength, it is advisable to retrain the model to ensure optimal segmentation performance. Due to the need for manual intervention or empirically determined segmentation parameters (e.g., vesselness thresholds) in previous methods and the lack of T1w images in our study,

a direct and fair comparison of the segmentation accuracies between the proposed and aforementioned methods is difficult to make. However, the superiority of neural networks over conventional methods has been demonstrated in segmenting other tubular thin structures such as perivascular spaces, in which DSC, PPV, and SEN were close to what we obtained in the current study.[16]

Several methods have been proposed to account for partial-volume effects in quantification of venous diameter and/or susceptibility. However, none of the previous methods can be applied to the DMVs. The joint use of magnitude and phase method[19] can simultaneously estimate venous oxygen saturation and partial-volume fraction in straight veins that are approximately parallel to main magnetic field with an assumption that the field outside the vein equals zero. However, most DMVs are almost perpendicular to the main magnetic field, which creates a substantial field outside them. Furthermore, the relationship between partial-volume fraction estimated by joint use of magnitude and phase and the vessel radius is unclear. The CISSCO (Complex Image Summation around a Spherical or a Cylindrical Object) method[20,21] adds up complex MR signals around a vein and equates the complex sums to analytical formulas containing the unknown venous susceptibility and radius. The venous susceptibility and diameter can be obtained by solving the equations. However, due to the low SNR of the phase variations surrounding the DMVs and the large covariance between susceptibility and diameter errors, reliable quantification of DMV diameters cannot be obtained using CISSCO. Furthermore, the effect of PSF was not considered in their equations either. Recently, multi-compartment QSM methods have been proposed.[31] To separate the different magnetic sources, different transverse relaxation rates of the compartments were considered. However, the venous compartment has not been included in the model.

The PSF formula described by Eq. (4) is derived under the assumption that the image is obtained by discrete inverse Fourier transform of fully sampled k-space data. However, for undersampled acquisitions, the reconstruction process often involves certain types of regularization, which may result in discrepancies between the actual PSF and the one assumed in Eq. (4). On the other hand, filters applied during image reconstruction such as antiringing filter can also affect the PSF and should be avoided in order to apply the proposed method. For a given reconstruction pipeline, the actual PSF can potentially be estimated by reconstructing k-space data with a constant and uniform value across the entire sampled k-space domain.

We note that in the current method, the susceptibility of venous blood ($\Delta\chi$) is fixed to a typical value of 0.41 ppm, to reduce the number of fitting parameters and to improve the robustness of the fitted results to noise. In the phantom study, the fitted diameter exhibited a $1/\sqrt{\Delta\chi}$ dependence (Figure 4A), suggesting that $\Delta\chi$ and the diameter cannot be reliably determined simultaneously from the fit, and a separate method for determining $\Delta\chi$ is needed. In previous studies,[20,32,33] the average $\Delta\chi$ value of healthy subjects has been reported to lie within the range of 0.33 and 0.54 ppm. Furthermore, some studies have demonstrated that some specific diseases (e.g., hemodialysis[32] and leukoencephalopathy[34]) are associated with the decrease of patients' venous oxygen saturation, which will be reflected in the increase of $\Delta\chi$. Assuming a broader $\Delta\chi$ value range extending from 0.33 to 0.60 ppm, we can deduce that the reported DMV diameters may introduce a bias ranging from −17.3% to 11.5%, based on the results demonstrated in Figure 4A (i.e., the estimated diameters scale with $1/\sqrt{\Delta\chi}$). To determine whether there exists susceptibility alterations in venous blood, the proposed method can be extended to include the susceptibility of venous blood as a free-fitting parameter and apply it to straight large veins downstream to DMV, such as the septal veins, where the contrast-to-noise ratio is higher, as we have demonstrated in an earlier study.[35]

Our simulation study suggests that the DMV diameters derived from model fitting are overestimated when the voxel size is above 0.45 mm. The origin of the overestimation remains to be determined but may be caused by the difficulty of the model to accurately locate the specific spatial position of the vessel based on the numerical data with lower resolution. We note that the resolution for the in vivo study ($0.43 \times 0.43 \times 0.4 \, mm^3$) is within the range with relatively small errors.

Narrowing of DMVs due to collagenosis can reduce blood flow into deep WM, which may lead to chronic ischemia and development of WM lesions. However, whether or not DMV dysfunction plays a role in the SVD etiopathogenesis remains unclear.[2,14,36–38] Large numbers of DMV can be visualized in SWI from high-field MRI at 3 T and 7 T, providing an opportunity for elucidating its role in SVD etiopathogenesis. Earlier studies reported greater number of DMV voxels in patients who had WM hyperintensities in T_2-weighted MR images than in healthy controls.[14] However, reduced DMV visibility has also been reported to be associated with increased severity of CSVD.[9,10,18,39] On the other hand, increased tortuosity of the DMV has been observed in patients with early Alzheimer's disease and amnestic mild cognitive impairment.[38] However, the underlying physiological changes of the DMVs underlying those morphological observations remain to be determined.

The automatic segmentation model developed in this study can facilitate future studies into the earlier morphological changes that may take place before the onset of cognitive impairments. Furthermore, quantitative

evaluation of DMV diameters can help distinguish whether changes in the inner diameters of DMVs, changes in deoxyhemoglobin levels, or both gives rise to changes in DMV conspicuity in patients with CSVD.

6 | CONCLUSIONS

A new method is developed to segment DMVs automatically and to quantitatively measure DMV diameters. The phantom study demonstrated that the quantification method can accurately correct for partial-volume effects and obtain diameters close to the true values. The trained automatic segmentation model based on 3D-UNet provided by the nnU-Net framework can extract DMVs from GRE data accurately. DMV diameters measured by our method across 20 subjects were distributed primarily in the 90–200 μm range. The proposed method may facilitate the study of the role of DMV in the pathogenesis of CSVD.

DATA AVAILABILITY STATEMENT
The in vivo images, ground truth masks, trained model, and MATLAB codes for DMV diameter measurement are available in Mendeley Data (https://data.mendeley.com/datasets/8z3x7cscs3/1).

ORCID
Yichen Zhou https://orcid.org/0009-0000-3888-0224
Bingbing Zhao https://orcid.org/0009-0001-1638-0736
Xiaopeng Zong https://orcid.org/0000-0003-4235-6948

REFERENCES
1. Moody DM, Brown WR, Challa VR, Anderson RL. Periventricular venous collagenosis: association with leukoaraiosis. *Radiology*. 1995;194:469-476.
2. Keith J, Gao FQ, Noor R, et al. Collagenosis of the deep medullary veins: an underrecognized pathologic correlate of white matter hyperintensities and periventricular infarction? *J Neuropathol Exp Neurol*. 2017;76:299-312.
3. Wang JY, Li JY, Luo D, et al. Extracellular vesicles play a central role in cerebral venous disease-associated brain atrophy. *Adv Sci*. 2023;10:2301574.
4. Haacke EM, Mittal S, Wu Z, Neelavalli J, Cheng YCN. Susceptibility-weighted imaging: technical aspects and clinical applications, part 1. *Am J Neuroradiol*. 2009;30:19-30.
5. Li M, Hu J, Miao Y, et al. In vivo measurement of oxygenation changes after stroke using susceptibility weighted imaging filtered phase data. *PLoS One*. 2013;8:e63013.
6. Haacke EM, Tang J, Neelavalli J, Cheng YCN. Susceptibility mapping as a means to visualize veins and quantify oxygen saturation. *J Magn Reson Imaging*. 2010;32:663-676.
7. Xu B, Liu T, Spincemaille P, Prince M, Wang Y. Flow compensated quantitative susceptibility mapping for venous oxygenation imaging. *Magn Reson Med*. 2013;72:438-445.
8. Hooshmand I, Rosenbaum AE, Stein RL. Radiographic anatomy of normal cerebral deep medullary veins: criteria for distinguishing them from their abnormal counterparts. *Neuroradiology*. 1974;7:75-84.
9. Chen X, Wei L, Wang J, et al. Decreased visible deep medullary veins is a novel imaging marker for cerebral small vessel disease. *Neurol Sci*. 2020;41:1497-1506.
10. Ao DH, Zhang DD, Zhai FF, et al. Brain deep medullary veins on 3-T MRI in a population-based cohort. *J Cereb Blood Flow Metab*. 2021;41:561-568.
11. Zhang R, Zhou Y, Yan S, et al. A brain region-based deep medullary veins visual score on susceptibility weighted imaging. *Front Aging Neurosci*. 2017;9:269.
12. Tian Y, Li S, Yang Y, et al. Associations of deep medullary veins with vascular risk factors, laboratory indicators, and cerebral small vessel disease: a population-based study. *Brain Behav*. 2023;13:e2974.
13. Kuijf HJ, Bouvy WH, Zwanenburg JJM, et al. Quantification of deep medullary veins at 7 T brain MRI. *Eur Radiol*. 2016;26:3412-3418.
14. Yan S, Wan J, Zhang X, et al. Increased visibility of deep medullary veins in leukoaraiosis: a 3-T MRI study. *Front Aging Neurosci*. 2014;6:144.
15. Jeong J-W, Lee MH, Luat AF, Xuan Y, Haacke EM, Juhász C. Quantification of enlarged deep medullary vein volumes in Sturge-Weber syndrome. *Quant Imaging Med Surg*. 2024;14:1916-1929.
16. Lian C, Zhang J, Liu M, et al. Multi-channel multi-scale fully convolutional network for 3D perivascular spaces segmentation in 7T MR images. *Med Image Anal*. 2018;46:106-117.
17. Xu Z, Li F, Wang B, et al. New insights in addressing cerebral small vessel disease: association with the deep medullary veins. *Front Aging Neurosci*. 2020;12:597799.
18. Zhou Y, Li Q, Zhang R, et al. Role of deep medullary veins in pathogenesis of lacunes: longitudinal observations from the CIRCLE study. *J Cereb Blood Flow Metab*. 2020;40:1797-1805.
19. McDaniel P, Bilgic B, Fan AP, Stout JN, Adalsteinsson E. Mitigation of partial volume effects in susceptibility-based oxygenation measurements by joint utilization of magnitude and phase (JUMP). *Magn Reson Med*. 2017;77:1713-1727.
20. Hsieh CY, Cheng YCN, Xie H, Haacke EM, Neelavalli J. Susceptibility and size quantification of small human veins from an MRI method. *Magn Reson Imaging*. 2015;33:1191-1204.
21. Hsieh CY, Cheng YCN, Neelavalli J, Haacke EM, Stafford RJ. An improved method for susceptibility and radius quantification of cylindrical objects from MRI. *Magn Reson Imaging*. 2015;33:420-436.
22. Chu KC, Xu Y, Balschi JA, Springer Jr. CS. Bulk magnetic susceptibility shifts in nmr studies of compartmentalized samples: use of paramagnetic reagents. *Magn Reson Med*. 1990;13(2):239–262.

23. Haacke EM, Lai S, Reichenbach JR, et al. In vivo measurement of blood oxygen saturation using magnetic resonance imaging: a direct validation of the blood oxygen level-dependent concept in functional brain imaging. *Hum Brain Mapp*. 1997;5:341-346.

24. Wang Y, Liu T. Quantitative susceptibility mapping (QSM): decoding MRI data for a tissue magnetic biomarker. *Magn Reson Med*. 2015;73:82-101.

25. Kadamangudi S, Reutens D, Sood S, Vegh V. Signal compartments in ultra-high field multi-echo gradient echo MRI reflect underlying tissue microstructure in the brain. *Neuroimage*. 2018;178:403-413.

26. Sousa MC, Buchanan JW. Observational models of graphite pencil materials. *Comput Graphics Forum*. 2001;19:27-49.

27. Liao S, Mo Z, Zeng M, et al. Fast and low-dose medical imaging generation empowered by hybrid deep-learning and iterative reconstruction. *Cell Rep Med*. 2023;4:101119.

28. Zong X, Lian C, Jimenez J, Yamashita K, Shen D, Lin W. Morphology of perivascular spaces and enclosed blood vessels in young to middle-aged healthy adults at 7T: dependences on age, brain region, and breathing gas. *Neuroimage*. 2020;218:116978.

29. Isensee F, Jaeger PF, Kohl SAA, Petersen J, Maier-Hein KH. nnU-net: a self-configuring method for deep learning-based biomedical image segmentation. *Nat Methods*. 2021;18:203-211.

30. Jolliffe IT. Principal Component Analysis. Springer Series in Statistics. 2002. New York: Springer.

31. Li Z, Feng R, Liu Q, et al. APART-QSM: an improved sub-voxel quantitative susceptibility mapping for susceptibility source separation using an iterative data fitting method. *Neuroimage*. 2023;274:120148.

32. Chai C, Liu S, Fan L, et al. Reduced deep regional cerebral venous oxygen saturation in hemodialysis patients using quantitative susceptibility mapping. *Metab Brain Dis*. 2017;33:313-323.

33. Fan AP, Bilgic B, Gagnon L, et al. Quantitative oxygenation venography from MRI phase. *Magn Reson Med*. 2014;72:149-159.

34. Ling C, Zhang Z, Wu Y, et al. Reduced venous oxygen saturation associates with increased dependence of patients with cerebral autosomal dominant arteriopathy with subcortical infarcts and leukoencephalopathy. *Stroke*. 2019;50:3128-3134.

35. Zong X, Lin W. Quantitative measurements of deep medullary vein caliber and oxygenation level using MRI phase and complex images. *In: Proceedings of the 26th Annual Meeting of ISMRM*, Paris, France, 2018; 26: 0269.

36. Hartmann DA, Hyacinth HI, Liao FF, Shih AY. Does pathology of small venules contribute to cerebral microinfarcts and dementia? *J Neurochem*. 2017;144:517-526.

37. Brown WR, Moody DM, Challa VR, Thore CR, Anstrom JA. Venous collagenosis and arteriolar tortuosity in leukoaraiosis. *J Neurol Sci*. 2002;203-204:159-163.

38. Bouvy WH, Kuijf HJ, Zwanenburg JJ, et al. Abnormalities of cerebral deep medullary veins on 7 Tesla MRI in amnestic mild cognitive impairment and early Alzheimer's disease: a pilot study. *J Alzheimers Dis*. 2017;57:705-710.

39. Wang X, Lyu J, Duan Q, et al. Deep medullary vein damage correlates with small vessel disease in small vessel occlusion acute ischemic stroke. *Eur Radiol*. 2024;34:6026-6035.